An instrumental electrode model for solving EIT forward problems

An instrumental electrode model for solving EIT forward problems

Weida Zhang[1,2] and David Li[1,3]

[1] Department of Engineering and Design, School of Engineering and Informatics, University of Sussex, BN1 9SB, UK
[2] Department of Electronic Engineering, School of Information and Electronics, Beijing Institute of Technology, 100081, People's Republic of China
[3] Strathclyde Institute of Pharmacy and Biomedical Sciences, University of Strathclyde, G4 0RE, Scotland, UK

E-mail: wz39@sussex.ac.uk and david.li@strath.ac.uk

Abstract

An instrumental electrode model (IEM) capable of describing the performance of electrical impedance tomography (EIT) systems in the MHz frequency range has been proposed. Compared with the commonly used Complete Electrode Model (CEM), which assumes ideal front-end interfaces, the proposed model considers the effects of non-ideal components in the front-end circuits. This introduces an extra boundary condition in the forward model and offers a more accurate modelling for EIT systems. We have demonstrated its performance using simple geometry structures and compared the results with the CEM and full Maxwell methods. The IEM can provide a significantly more accurate approximation than the CEM in the MHz frequency range, where the full Maxwell methods are favoured over the quasi-static approximation. The improved electrode model will facilitate the future characterization and front-end design of real-world EIT systems.

Keywords: electrical impedance tomography (EIT), complete electrode model, instrumental EIT, finite elements, EIDORS, non-ideal front-ends

(Some figures may appear in colour only in the online journal)

1. Introduction

Electrical impedance tomography (EIT) (Barber and Brown 1984, Cheney *et al* 1999, Holder 2005, Metherall *et al* 1996, Saulnier *et al* 2001, Webster 1990), is a technique for determining

the distribution of the conductivity or admittivity in a volume by injecting electrical currents into the volume and measuring the corresponding potentials on the surface of the volume. A 3D image of the conductivity distribution is generated by using inverse algorithms, which includes a so-called forward problem capable of predicting the voltages on defined surface electrodes for a given conductivity distribution (Lionheart 2004).

EIT has been applied to cancer diagnosis applications. It is desirable to operate in the 0.1–10 MHz band since a difference in admittivity between malignant and normal tissues can be observed in this frequency range (Grimnes and Martinsen 2008, Schwan 1957, Surowiec *et al* 1988). Recently, several image reconstruction methods have been proposed to enhance the EIT contrast, but only in the frequency range of tens of kHz (Ahn *et al* 2010, Harrach *et al* 2010, Jun *et al* 2009, Seo *et al* 2008). There are two major problems in extending the operating frequency of EIT systems. Firstly, it is difficult to obtain accurate measurements from experimental devices when the operating frequency increases. The instrumental effects including non-idealities of the sources, measurement devices and parasitic capacitance (from the cables, connectors or the electrodes themselves), etc., start to degrade the measurement accuracy at frequencies larger than hundreds of kHz. Secondly, the Laplace equation used by the EIT forward problem is an approximation derived from Maxwell's equations (Boyse *et al* 1992, Boyse and Paulsen 1997, Paulsen *et al* 1992, Soni *et al* 2006). The 'irrotational electric field' approximation tends to fail when the frequency increases, as the quasi-static assumption is no longer valid (Sheng and Song 2012).

For the first problem, we found that the boundary conditions (BCs) used for forward problems are not sufficient for system modelling in the low MHz band. There are different kinds of BCs used in the EIT forward problems, including the Gap Model (Boyle and Adler 2010), Shunt Electrode Model (Boyle and Adler 2010) and Complete Electrode Model (CEM) (Boyle and Adler 2010, Cheng *et al* 1989, Somersalo *et al* 1992, Vauhkonen *et al* 1999). The CEM constrains the electrical currents flowing on the electrode surfaces and on the boundary of the imaging volume. It also includes the contact impedance on the electrode surface and therefore accounts for the voltage difference between the electrode and the outer surface of the imaging volume. It has been reported that the CEM can match experimental results with a very high precision up to 0.1 % (Somersalo *et al* 1992). To reconstruct accurate images from in vivo data an accurate electrode model is usually required, and thus, the CEM is generally preferred (Boyle and Adler 2010). The accuracy of CEM solutions depends on accurate measurements or estimations of the contact impedance. Methods and results have been reported to estimate the contact impedance for CEM (Boverman *et al* 2007, Demidenko 2011, Demidenko *et al* 2011).

The CEM, however, assumes that the system hardware is ideal and therefore does not consider the loading effects of the current excitation sources or the voltage measurement components. This assumption is only valid at frequencies much lower than 1 MHz. Several research groups have described design implementations, simulations and experiment results using hardware with current source output impedances measured in MΩ at frequencies up to hundreds of kHz (Denyer *et al* 1994). Usually the input impedance of the front-end amplifiers in voltage measurement components (such as op-amp follower (Oh *et al* 2011) or instrumentation amplifier (Oh *et al* 2007a)) is around several GΩ.

To overcome the first problem, the requirements for high output/input impedance of the excitation/measurement circuits pose a significant challenge in hardware implementation, especially at high frequencies, and therefore impose a limitation on the effective use of the forward model. Recent research efforts have been devoted to enhancing the output impedance of current sources, such as using driven shields and generalized impedance converters (GIC) (Ross *et al* 2003). It has been shown that a GIC can increase the output impedance up to 2 MΩ at 495 kHz (Oh *et al* 2011). Another method for modelling and optimising the hardware of EIT systems has been proposed (Hartinger *et al* 2006) using a Howland current source and a bootstrapped

follower to model the hardware effects and optimise the parameters of the circuit, but it only improved the performance at frequencies less than 100 kHz. An image reconstruction method has been reported in which hardware effects were modelled through modification of the system matrix used for the inversion (Hartinger *et al* 2007). However, the reported operating frequency was much lower than 500 kHz as there was no optimisation of the forward model.

For the quasi-static approximation, which is the second problem mentioned earlier, a finite element analysis method derived from the full Maxwell equations (called the $\mathbf{A} - \Phi$ formulation) has been proposed (Soni *et al* 2006) and the formulations (which did not apply the quasi-static assumption) have been applied to voltage source based systems operating up to 10 MHz (Halter *et al* 2004, Halter *et al* 2008). Being derived from the full Maxwell equations, the formulation is very computationally intensive compared to a Laplace formulation. A calibration method is used for compensating the instrumental effects (which also appear in voltage source systems).

Several calibration algorithms have been proposed for correcting the measurement errors caused by hardware non-idealities (Halter *et al* 2008, Holder 2005, McEwan *et al* 2006, Oh *et al* 2007a). These effectively compensate the instrumental effect on driving electrodes but it is difficult to remove all instrumental effects (including measuring electrode error) in the frequency range we are considering.

The proposed instrumental electrode model (IEM) considers the effects on the potential distribution in the volume caused by hardware non-idealities, especially at frequencies larger than 500 kHz. An extra boundary condition is introduced accordingly to the CEM in the forward problem. The IEM can provide a much more accurate representation of the overall system including instrumental effects introduced by the hardware (the first problem mentioned).

It is worth noting that although the two previously mentioned effects are normally combined when operating in the MHz frequency range, they do not always occur together. The instrumental effect is due to hardware non-idealities and depends on the parameters of the hardware alone, while the full Maxwell effect is caused by the quasi-static assumption and depends on the admittivity and permeability of the material and the overall system geometry and scale size.

In this paper, we will derive the IEM forward model and compare with the results obtained from the CEM, from $\mathbf{A} - \Phi$ formulations (derivations for 3D problems are attached in appendix A based on the equations for 2D problems derived in Soni *et al* (2006)) and from COMSOL Multiphysics (commonly used commercial Maxwell solvers) to assess the comparative performance over the frequency range of interest.

The paper is organized as follows. Section 2 describes the forward problem formulation as usually applied in EIT. The IEM is detailed in section 3 based on the CEM. A lumped-circuit model and a tank model are solved by the above methods in section 4 and their results are cross-compared and discussed. The conclusions are presented in section 5.

The paper is mainly focused on current source EIT systems. We believe that the instrumental non-idealities would bring similar impacts to both current source and voltage source EIT systems based on circuit theory. Demonstrating such impacts on a current source system should be able to shed a light on how instrumental non-idealities deteriorate system performances. The IEM formula for typical voltage source systems, however, is also derived with an example included in the appendix B, as voltage source systems are also widely used.

2. Forward problem

The forward problem for the volume under consideration can be formulated from Maxwell's equations,

$$\nabla \times \mathbf{E} = -\mathrm{i}\omega\mu\mathbf{H}, \tag{2.1a}$$

$$\nabla \times \mathbf{H} = \mathbf{J} + i\omega\varepsilon\mathbf{E}, \tag{2.1b}$$

where $\mathbf{E}$ is the electric field, $\mathbf{H}$ is the magnetic field, ω is the angular frequency, μ and ε are the electrical permittivity and magnetic permeability respectively, and $\mathbf{J} = \sigma\mathbf{E}$ with σ being the conductivity. With the complex permittivity or so-called admittivity, $\varepsilon^* = \sigma + i\omega\varepsilon$, substituted in the equation (2.1b) we have

$$\nabla\cdot(\nabla\times\mathbf{H}) = \nabla\cdot(\sigma\mathbf{E} + i\omega\varepsilon\mathbf{E}) = \nabla\cdot(\varepsilon^*\mathbf{E}) = 0. \tag{2.2}$$

As electric fields often contain singularities, electric potentials are used instead. In computational electromagnetics (Sheng and Song 2012), the electric potential Φ is also called the scalar potential in contrast with the vector potential $\mathbf{A}$ or magnetic potential which are defined as

$$\mathbf{B} = \nabla \times \mathbf{A},$$
$$\mathbf{E} = -\nabla\Phi - i\omega\mathbf{A}. \tag{2.3}$$

The electric field $\mathbf{E}$ consists of an irrotational part ($\nabla\Phi$) and a rotational part ($i\omega\mathbf{A}$). From equation (2.2) and equation (2.3), we obtain

$$0 = \nabla\cdot\varepsilon^*(\nabla\Phi + i\omega\mathbf{A}). \tag{2.4}$$

The vector potential is usually ignored in EIT systems, considering the operating frequency or the geometric scale of the problem. The Maxwell equation is therefore reduced to a Laplace equation at low frequencies using the well-known quasi-static approximation,

$$\nabla\cdot\varepsilon^*(\nabla\Phi + i\omega\mathbf{A}) \simeq \nabla\cdot\varepsilon^*\nabla\Phi = 0. \tag{2.5}$$

Equation (2.5) is the governing equation for EIT systems. Many experimental results have been presented (Halter *et al* 2008, Holder 2005) which demonstrate that the approximation performs equivalently to the full Maxwell solutions at low frequencies.

3. Boundary conditions and numerical solutions

3.1. IEM boundary conditions

To solve the partial differential equation (2.5), proper boundary conditions should be applied to describe the current injection and model the behaviour of electrodes. The CEM (Cheng *et al* 1989, Somersalo *et al* 1992, Vauhkonen *et al* 1999) is commonly used and has been experimentally proven to be accurate in low frequency EIT systems. The proposed IEM is based on the CEM, but instrumental non-ideality is given additional consideration within the electrode model. These boundary conditions can be understood from figure 1. Here we use a current source EIT system for this demonstration, and for those who interested in voltage source systems please see the appendix B.

Referring to the EIT electrode model in figure 1, each electrode can be configured either as a driving electrode (with the switch closed and the current source connected to the electrode) or as a measuring electrode (with the switch opened and the current source disconnected). The current source has an output impedance $\mathbf{Z}_O$ with the electrode contributing some parasitic capacitance $\mathbf{C}_S$ to ground, and the measurement circuit can be modelled with an input impedance $\mathbf{Z}_I$. The current source generates a current of I_{Sl}.

In the ideal situation, $\mathbf{Z}_O$ and $\mathbf{Z}_I$ are assumed to be infinite, $\mathbf{C}_S$ to be zero, and all of the current generated from the source goes into the electrode, $I_{Sl} = I_l$, when the switch is closed. When the switch is opened (the circuit acts as a measurement circuit), $I_l = 0$.

The frequency of interest for many EIT applications extends up to several MHz, and difficulties therefore emerge when applying the CEM. Some of the assumptions in the ideal situation mentioned above need to be re-examined and modified, since non-ideal loading effects are not negligible in the MHz frequency range.

Firstly, the output impedance $\mathbf{Z}_O$ of the current source and input impedance $\mathbf{Z}_I$ of the measurement circuit are not infinitely high. The circuit front-ends can easily contribute a few pF of parasitic capacitance contributed by the devices, therefore reducing input/output impedances and degrading the performance in the MHz range. In addition the parasitic capacitance of the cable, PCB trace and electrode itself (modelled by $\mathbf{C}_S$ in general) is not negligible. Although $\mathbf{C}_S$ almost remains constant across the frequency range, the equivalent impedance of the capacitance $1/(i\omega\mathbf{C}_S)$ reduces and starts loading the front-ends as the frequency increases.

At high frequencies, the electrode current flows therefore behave differently. In contrast to the assumption made by the CEM, at high frequencies some portion of I_{Sl} flows through $\mathbf{Z}_O$, $\mathbf{Z}_I$ and $\mathbf{C}_S$ (this part is negligible when the frequency is low) rather than entirely into the electrode. Also, for electrodes in measuring mode (with the switch open), there is some current flowing through $\mathbf{Z}_I$ and $\mathbf{C}_S$ to ground, as I_l, even though there is no driving current I_{Sl}.

Analytical calculations based on typical circuit parameters provide some indication of typical input and output impedances. When the operating frequency is 1 MHz, the output impedance $\mathbf{Z}_O$ typically comprises a resistance of 5 MΩ in parallel with a capacitance of 4 pF and the input impedance $\mathbf{Z}_I$ comprises a resistance of 10 MΩ in parallel with a capacitance 4 pF (This comes from an easily accessible front-end amplifier, for example, 4.5 pF from the Analog Devices AD8065 or 6 pF from the Texas Instruments OPA2365.) and a parasitic capacitance $\mathbf{C}_S$ of 2 pF. At 1 MHz, the overall instrumental effect is modelled with a virtual impedance $\mathbf{Z}_F$, as shown in figure 1, and becomes 16 kΩ in driving mode and 26 kΩ in measuring mode, which is *far* from infinite.

For EIT systems working at lower frequencies (< 500 kHz), the GIC (Oh *et al* 2011, Oh *et al* 2007b, Ross *et al* 2003) is widely used to alleviate the effects of capacitive loading, but it performs poorly at frequencies higher than 500 kHz.

From the above calculations, it is obvious that there is a significant 'leakage current' flowing through the instrumental path (with an equivalent impedance of $\mathbf{Z}_F$) from the current source (in the driving mode) or from the imaging volume (in the measuring mode) and for accurate representation this leakage current must be included when solving the system matrix.

We can reformulate the electrode model to include the 'leakage currents' in the forward problem. We obtain, in the driving mode,

$$I_{Sl} + \frac{V_l - V_{GND}}{\mathbf{Z}_F} + I_l = 0,$$

and in the measuring mode,

$$\frac{V_l - V_{GND}}{\mathbf{Z}_F} + I_l = 0,$$

combined as

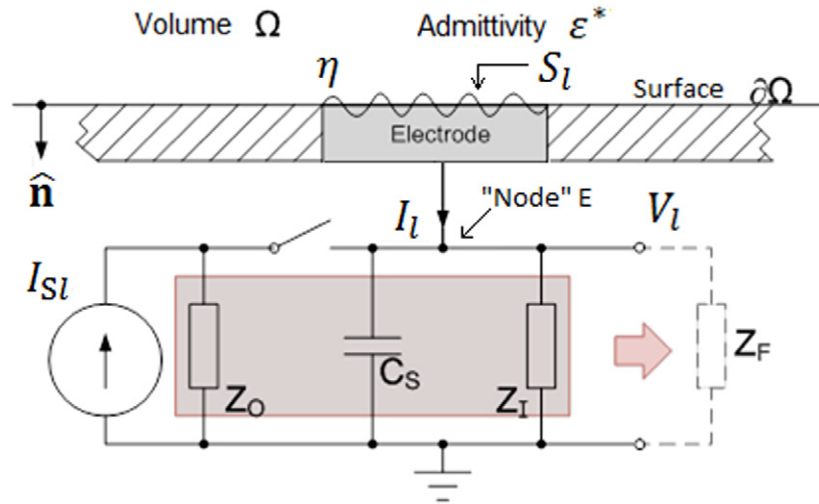$$I_{Sl} + \frac{V_l}{\mathbf{Z}_F} + I_l = 0. \tag{3.1}$$

Figure 1. EIT electrode geometry and circuit model.
where Ω is the volume to be solve,

$\partial\Omega$ is the surface of the volume,

E is a designator for the electrode circuit node,

$\hat{\mathbf{n}}$ is the outward normal vector on the volume surface,

S_l is the surface of the lth electrode,

I_l is the current of the lth electrode,

η is the contact impedance in $\Omega \cdot m^2$,

V_l is the voltage measured on the lth electrode,

I_{Sl} is the current output by the source, connected with the lth electrode,

$\mathbf{C_S}$ is the total parasitic capacitance of the cable, PCB trace and electrode itself,

$\mathbf{Z_O}$ is the output impedance of the current source,

$\mathbf{Z_I}$ is the input impedance of the voltage measurement device,

and $\mathbf{Z_F}$ is the virtual impedance, equivalent to the total effect of the above impedance.
For the remaining symbols in the figure we kept the previous definitions.

Together with the CEM BCs, we have the IEM as

$$\varepsilon^*\nabla\Phi\cdot\hat{\mathbf{n}} = 0 \quad \text{(Surface not on electrodes)}, \tag{3.2a}$$

$$\int_{S_l} \varepsilon^*\nabla\Phi\cdot\hat{\mathbf{n}}\,dS = I_l \quad \text{(Surface on lth electrode)}, \tag{3.2b}$$

$$\Phi + \eta\varepsilon^*\nabla\Phi\cdot\hat{\mathbf{n}} = V_l, \tag{3.2c}$$

$$I_{Sl} + \frac{V_l}{\mathbf{Z_F}} + I_l = 0,$$

$$\sum_{l=1}^{L} I_l = 0. \tag{3.2d}$$

Note that, with the external circuit attached, the total current generated from current sources $\sum_{l=1}^{L} I_{Sl}$ may not be balanced any more (as $\mathbf{Z_F}$ on different driving electrodes may vary), but the total charge in the volume to be solved $\sum_{l=1}^{L} I_l$ has to be zero.

In our IEM formulations, the potential balance condition $\sum_{l=1}^{L} V_l$ used in CEM is removed. As the CEM does not have a reference ground, whereas the IEM embeds one in the instrumental circuit.

When the operating frequency is low enough, the current flowing through the instrumental path $\mathbf{Z}_F$ is negligible, in which case the IEM will behave just like the CEM.

The IEM provides a method for describing non-ideal hardware behaviours and is therefore able to obtain accurate solutions of the forward problem with knowledge of the hardware, unlike the CEM which assumes perfect hardware.

3.2. Numerical modelling with IEM

Finite element methods (FEM) are used for solving the forward model with the IEM. Our programs were developed based on the software package EIDORS (Electrical Impedance and Diffuse Optical Reconstruction Software). EIDORS is a Matlab toolkit for three-dimensional EIT (Adler and Lionheart 2006, Polydorides and Lionheart 2002, Soleimani *et al* 2005). To apply our IEM model, similar formulations were derived, but with modifications.

We use equation (2.5) and the IEM derived in section 3 as our formulations. Applying the vector derivative identity, Green's identity and divergence theorem, we obtain the weak form:

$$\int_{\Omega} \varepsilon^* \nabla v \cdot \nabla \Phi \mathrm{d}V = \int_{\partial\Omega} v\varepsilon^* \nabla \Phi \cdot \hat{\mathbf{n}} \mathrm{d}S, \tag{3.3}$$

where v is an arbitrary test function.

With the Non-Electrode surface BC equation (3.2a) included,

$$\int_{\Omega} \varepsilon^* \nabla v \cdot \nabla \Phi \mathrm{d}V = \sum_{l=1}^{L} \int_{S_l} v\varepsilon^* \nabla \Phi \cdot \hat{\mathbf{n}} \mathrm{d}S. \tag{3.4}$$

Two unknowns are added to the system equations; one of them is V_l, the potential on electrode circuit 'node E', and the other is I_l, the current through the volume to be solved. Equation (3.2c) is used to add the extra unknown V_l,

$$\int_{\Omega} \varepsilon^* \nabla v \cdot \nabla \Phi \mathrm{d}V + \sum_{l=1}^{L} \frac{1}{\eta} \int_{S_l} v\Phi \mathrm{d}S - \sum_{l=1}^{L} \frac{V_l}{\eta} \int_{S_l} v\mathrm{d}S = 0. \tag{3.5}$$

To constrain V_l, we substitute equation (3.2c) into equation (3.2b) to derive extra equations for V_l with the other unknown I_l involved, hence,

$$\int_{S_l} \frac{V_l - \Phi}{\eta} \mathrm{d}S - I_l = 0. \tag{3.6}$$

To constrain I_l, we have the additional equation (3.1), with the known instrument impedance as the factor,

$$\frac{V_l}{\mathbf{Z}_F} + I_l = -I_{Sl}. \tag{3.7}$$

Imposing the constraint of charge balance, equation (3.7) becomes

$$\frac{V_L}{\mathbf{Z}_F} - \sum_{l=1}^{L-1} I_l = -I_{SL}. \tag{3.8}$$

Finally, we obtain

$$\int_{\Omega} \varepsilon^* \nabla v \cdot \nabla \Phi \mathrm{d}V + \sum_{l=1}^{L} \frac{1}{\eta} \int_{S_l} v \Phi \mathrm{d}S - \sum_{l=1}^{L} \frac{V_l}{\eta} \int_{S_l} v \mathrm{d}S = 0,$$

$$\int_{S_l} \frac{V_l - \Phi}{\eta} \mathrm{d}S - I_l = 0,$$

$$\frac{V_l}{\mathbf{Z}_F} + I_l = -I_{Sl}, \qquad l = 1, 2, \cdots L - 1,$$

$$\frac{V_L}{\mathbf{Z}_F} - \sum_{l=1}^{L-1} I_l = -I_{SL}. \tag{3.9}$$

Using Galerkin's Method we insert the shape functions, $\Phi = \sum_{j=1}^{N} \phi_j u_j$ and $v = \phi_i$ in equation (3.9) and lead to the system matrix in the form

$$\begin{pmatrix} A + B & C & \mathbf{0}^{N \times L} \\ C^{\mathrm{T}} & D & -\mathbb{I}^{L \times L} \\ \mathbf{0}^{L \times N} & E & F \end{pmatrix} \begin{pmatrix} \mathbf{u} \\ \mathbf{v} \\ \mathbf{i} \end{pmatrix} = \begin{pmatrix} \mathbf{0}^{N \times 1} \\ \mathbf{0}^{L \times 1} \\ -\mathbf{i_S} \end{pmatrix},$$

$$A = \int_{\Omega} \varepsilon^* \nabla \phi_i \cdot \nabla \phi_j \mathrm{d}V, \in \mathbb{C}^{N \times N},$$

$$B = \sum_{l=1}^{L} \frac{1}{\eta} \int_{S_l} \phi_i \phi_j \mathrm{d}S, \in \mathbb{C}^{N \times N},$$

$$C = -\frac{1}{\eta} \int_{S_l} \phi_i \mathrm{d}S, \in \mathbb{C}^{N \times L},$$

$$D = \mathrm{diag} \left\{ \frac{S_l}{\eta} \right\}, \in \mathbb{C}^{L \times L},$$

$$E = \mathrm{diag} \left\{ \frac{1}{\mathbf{Z}_F} \right\}, \in \mathbb{C}^{L \times L},$$

$$F = \begin{bmatrix} 1 & 0 & \cdots & 0 & 0 \\ 0 & 1 & & 0 & 0 \\ \vdots & & \ddots & & \vdots \\ 0 & 0 & & 1 & 0 \\ -1 & -1 & \cdots & -1 & 0 \end{bmatrix}, \in \mathfrak{R}^{L \times L},$$

where $\mathbb{I}^{L \times L}$ is identity matrix, $\mathbf{u}^{N \times 1}$ is the nodal potential vector (made up with u_j), $\mathbf{v}^{L \times 1}$ is the electrode voltage vector (made up with V_l), $\mathbf{i}^{L \times 1}$ is the electrode current vector (made up with I_l), $\mathbf{i_S}^{L \times 1}$ is the source injection current vector (made up with I_{Sl}), $\phi_{i,j}$ is the shape functions, N is the total number of the vertices, and i, j are the index of vertices.

Compared with the CEM, our IEM adds the matrix $\mathbb{I}^{L \times L}$ providing extra freedom to the electrode current, and regulates the electrode current by E and F. When the frequency increases with the $\mathbf{Z}_F$ reduced, $E\mathbf{v}$ increases and therefore reduces the current applied on the products $C^{\mathrm{T}}\mathbf{u}$ and $D\mathbf{v}$ in the driving mode. For the measuring mode, (although the imposed source current I_{Sl} is zero) $E\mathbf{v} + F\mathbf{i}$ allows the current to flow through electrodes. While on the other hand, if the frequency is low, $\mathbf{Z}_F$ tends to infinity and the system matrix is equivalent to the CEM.
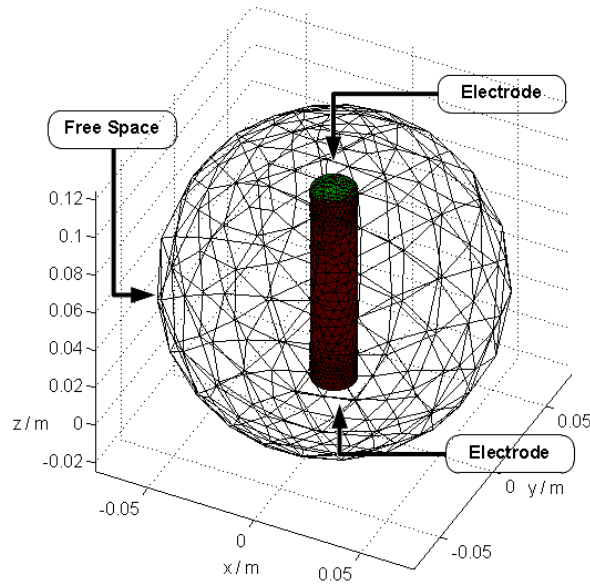
Figure 2. the geometry of the Lumped Model.

In addition, the process to find the ground node is removed, as the ground node is embedded in the IEM formulations.

4. Case studies and discussions

The following sections illustrate solutions of the forward model for two different geometry models and compare the results obtained using different solution methods.

4.1. Lumped model

The first geometry model, called 'Lumped Model,' is a cylinder with two electrodes at each end. The cylinder is filled with materials to simulate breast tissues (Surowiec *et al* 1988) and placed in free space as figure 2 defines.

In contrast to typical EIT models, the Lumped Model is clearly not able to predict the impedance distribution inside the volume without the prior knowledge of its homogeneity, as there are not enough electrodes. The free space outside the cylinder is usually ignored. The benefit of the Lumped Model is that as long as the free space (in the sphere) is removed, then it can be verified analytically by considering the model as a lumped circuit containing a parallel-plate capacitor C_S in parallel with a resistor R_S. As the material in the cylinder is homogeneous, the circuit components are given as

$$R_S = \frac{L}{\sigma S}, \quad C_S = \frac{\varepsilon S}{L}, \quad \mathbf{Z}_S = \frac{R_S \frac{1}{i\omega C_S}}{R_S + \frac{1}{i\omega C_S}} = \frac{L}{\varepsilon^* S},$$

where R_S, C_S and $\mathbf{Z}_S$ are the equivalent resistor, capacitor and impedance of the material, σ, ε and ε^* are the conductivity, permittivity and admittivity of the material, S is the surface area of the electrode (also the top/bottom surface area of the cylinder), L is the distance between the electrodes (also the length of the cylinder).
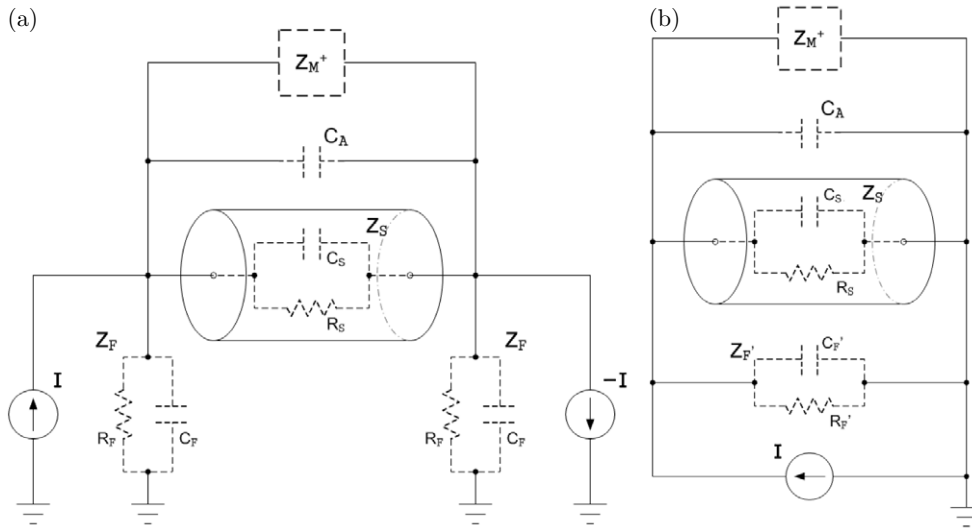
Figure 3. The equivalent circuit for Lumped Model. (*a*) For method (a)–(g). (*b*) For method (h) and (i).

In addition, on each electrode, a circuit unit consisting of a resistor R_F and a capacitor C_F can be attached to simulate the instrumental impedance $\mathbf{Z}_F$ we proposed in the IEM. Because there are only two electrodes in the model, current sources are applied on both of them in opposite direction and no measuring electrode is included.

When the surrounding free space is considered, the two electrodes form another capacitor (reflecting the interaction with the free space electric field) connected in parallel with $\mathbf{Z}_S$. We denote it as C_A or its reactance $\mathbf{X}C_A$, and solve it numerically.

As mentioned in the Introduction, the Laplace equations under the quasi-static approximation are not sufficient to obtain accurate solutions for the frequency range of interest. Here we denote the difference between the solutions obtained from the full Maxwell equations and the Laplace equations as the full Maxwell effect, and we use a circuit unit $\mathbf{Z}_{M^+}$ to model this effect although a simplistic equivalent impedance cannot fully represent this effect.

The equivalent circuit of the Lumped Model is shown in figure 3.

In our simulations, three main effects are included in the Lumped Model for solving the forward models. Note that we are not trying to quantify these effects, as they vary with geometries and materials, but merely to use the combinational effects to verify the IEM. These three effects are:

- Instrumental effect, $\mathbf{Z}_F$;
- Volume Cut-off effect, $\mathbf{X}C_A$;
- Full Maxwell's effect, $\mathbf{Z}_{M^+}$.

We obtained the simulation results by using the following nine methods (forward problem solvers or BCs sets) and cross-compared the results to assess the accuracy of the IEM implementation. The methods are:

(a) analytical lumped method

　An analytical solution based on an equivalent circuit of the cylinder and current sources.

(b) analytical lumped method with the instrumental effect $\mathbf{Z}_F$

　Similar to (a), but the instrumental impedance effect $\mathbf{Z}_F$ is also included in the analysis.

(c) CEM by EIDORs (Polydorides and Lionheart 2002) without considering the free space (no $\mathbf{X}C_A$)

An FEM forward model of the cylinder solved with the CEM. This models the potential distribution in the cylinder, contact impedance and the potentials on the two electrodes. Only the cylinder (coloured in dark red in figure 2) is meshed and solved without considering the surrounding free space (or $\mathbf{XC}_A$).

(d) CEM by EIDORs with $\mathbf{XC}_A$

Similar to (c), but with the free space (in figure 2) included and solved. Note that the governing equation (2.5) and the derivation in section 3.2 are free of sources inside the volume, which differs from the configuration for this simulation (the source electrodes are inside the finite elements volume). They are equivalent mathematically, but we do not need to detail the equations here.

(e) IEM without considering the free space (no $\mathbf{XC}_A$)

Similar to (c), but using the IEM we proposed in the section 3. It models the potential distribution in the cylinder, contact impedance on the two electrodes with the instrumental effect $\mathbf{Z}_F$ included.

(f) IEM with $\mathbf{XC}_A$

Similar to (e), but the free space ($\mathbf{XC}_A$) is included in the simulations.

(g) $\mathbf{A} - \Phi$ forward model in Helmholtz equations

An FEM forward model that solves the full Maxwell equations. It models the vector potential ($\mathbf{A}$) and scalar potential (Φ) distribution in the cylinder and also the surrounding free space shown in figure 2, but the contact impedance or instrumental effect is not considered. We derived the formula of the $\mathbf{A} - \Phi$ method based on a previously published 2D work (Soni *et al* 2006), and the data structure in Matlab is based on EIDORS using the mesh generating software NETGEN. A description of the forward model formulation can be found in the appendix.

(h) COMSOL Multiphysics without the instrumental effect $\mathbf{Z}_F$

The solution is obtained by COMSOL Multiphysics (well-known commercial finite-element software developed for solving differential equations in different applications, denoted as COMSOL hereafter). It models the electric field distribution in the cylinder and the surrounding free space (perfect matching layer, PML, is usually used in solving Maxwell's equations).

(i) COMSOL Multiphysics with $\mathbf{Z}_F$

Similar to (h), but we included the instrumental effect $\mathbf{Z}_F$ on electrodes.

Table 1 summarises the methods we used.

For all methods the dimensions of the cylinder, conductivity, permittivity, instrumental impedance, stimulation and frequencies are kept constant to allow fair comparison. The parameters are:

- Material conductivity, 0.03 S m^{-1}, (Surowiec *et al* 1988);
- Material relative permittivity, 40, (Surowiec *et al* 1988);
- Cylinder radius, 0.01 m;
- Cylinder length, 0.10 m;
- Current source driving current, 1 mA;
- Frequency range, 250 kHz–20 MHz.

Various other parameters apply to some of the individual methods:

- The equivalent impedance of the cylinder $\mathbf{Z}_S$ in (a) and (b) is calculated from the material property and cylinder dimension above.
- The resistive part of the instrumental impedance, R_F, in methods (b), (e) and (f) is 5 MΩ.
- The capacitive part of the instrumental impedance, C_F, in methods (b), (e) and (f) is 10 pF.

Table 1. List of the effects considered by each method.

Index	Name	Effect $\mathbf{Z}_F$	Effect $\mathbf{XC}_A$	Effect $\mathbf{Z}_{M^+}$
(a)	Analytical	No	No	No
(b)	Analytical w/$\mathbf{Z}_F$	**Yes**	No	No
(c)	CEM	No	No	No
(d)	CEM w/$\mathbf{XC}_A$	No	**Yes**	No
(e)	IEM	**Yes**	No	No
(f)	IEM w/$\mathbf{XC}_A$	**Yes**	**Yes**	No
(g)	$\mathbf{A}-\Phi$	No	**Yes**	**Yes**
(h)	COMSOL	No	**Yes**	**Yes**
(i)	COMSOL w/$\mathbf{Z}_F$	**Yes**	**Yes**	**Yes**

Note: The contact impedance in (c)–(f) is set to be $1 \times 10^{-6} \Omega \cdot m^2$ in order to compare with other methods which the contact impedance are not considered.

- The diameter of the free space sphere in methods (d), (f) and (g) is 0.15 m.
- The diameter of the free space plus PML sphere in method (h) and (i) is 0.15 m.
- Method (h) and (i) which uses COMSOL requires a uniform 'port' defined as field excitation, so the two opposing electrodes are considered as a single 'port', and the instrumental impedance, which is attached on each electrode in methods (b), (e) and (f), is combined into a single effective impedance connected in parallel with the port, as shown in figure 3(*b*) (with the impedance doubled to maintain equivalence with figure 3(*a*)).

figures 4 and 5 show the differential voltage in magnitude and phase obtained by the methods, (a)–(i).

Key findings from the various solution methods are as follows:

- The results from (a), analytical method, and (c), FEM with CEM BCs are almost the same, as they describe the same problem in analytical and numerical ways.
- The results from (b), analytical method with $\mathbf{Z}_F$, and (e), FEM with IEM BCs are in a good agreement, as they describe the same problem. And this shows our IEM describes the instrumental effect correctly.
- Both (b) and (e) start to attenuate at a much lower frequency than (a) and (c). This comes from the instrumental effect, where $\mathbf{Z}_F$ provides an extra path for the current and reduces the current injected into the cylinder.
- Similarly, the results for (d), FEM with CEM BCs and $\mathbf{XC}_A$, attenuate in magnitude at a lower frequency than the (a) and (c) results. This illustrates the volume cut-off effect. The capacitance contributed by the free space is not considered in (a) and is numerically chopped off in (c), which provides an extra path for the current.
- Similarly, the results for (f), FEM with IEM BCs and $\mathbf{XC}_A$, also shows the volume cut-off effect, but are not so different from the results for (b) and (e). This demonstrates that the instrument effect dominates in this case.
- The results for (g), FEM of $\mathbf{A}-\Phi$ problem with $\mathbf{XC}_A$, are very similar to the results for (d), FEM with CEM BCs and $\mathbf{XC}_A$. This shows that the full Maxwell effect $\mathbf{Z}_{M^+}$ is not obvious for the structure we chose in this frequency range.
- The (h) curves (obtained using COMSOL, but without considering $\mathbf{Z}_F$) are similar to the (d) curves, showing further that the Maxwell effect is not significant. The error between (g) and (h) will be discussed shortly.
- The results for (i) using COMSOL (including $\mathbf{Z}_F$) show the combined effects of $\mathbf{Z}_F$, $\mathbf{XC}_A$ and $\mathbf{Z}_{M^+}$, and they are close to the results for (f).
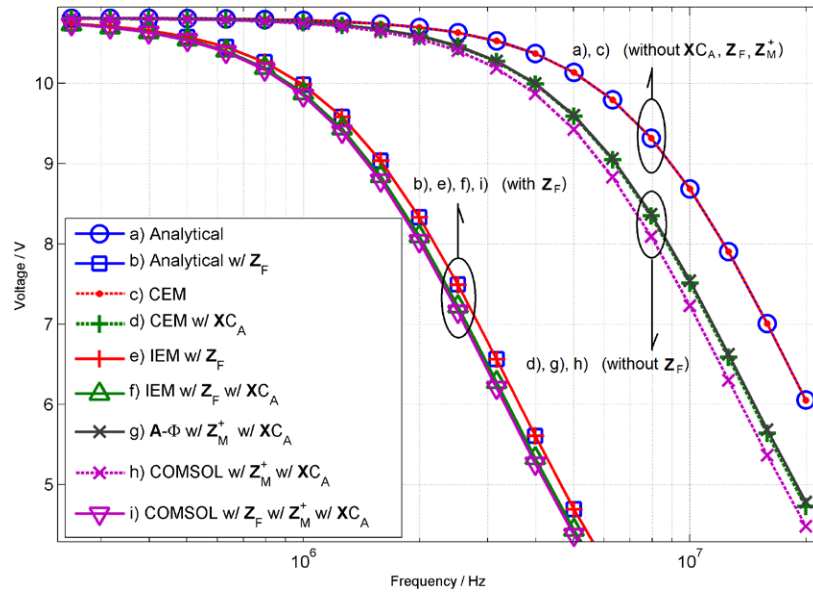
Figure 4. Solutions in magnitude of the forward problem obtained by using methods (a)–(i).

From the above, we conclude that:

- The numerical methods match the analytical methods perfectly; (a) with (c) and (b) with (e).
- The volume cut-off effect, XC_A, contributed by the free space surrounding the cylinder, is observable, based on the comparison between groups (d), (g) and (h) and groups (a) and (c) (groups are circled in the figures).
- The instrumental effect, Z_F, is significant. Based on comparisons between (a)–(c) and (e), (d) and (f), and (h) and (i) in both magnitude and phase plots.
- The Maxwell effect, Z_{M^+}, is insignificant, for the geometry and material property we chose.
- The two different Maxwell solvers (COMSOL and $A-\Phi$) give similar but not identical results. Both methods solve full Maxwell equations and are mathematically equivalent, and theoretically should obtain the same results. Potential reasons for the small discrepancy are:
  - In method (g), the $A-\Phi$ method solves Helmholtz equations with nodal FEM, as described in the appendix, while in method (h), COMSOL solves curl–curl equation (4.1) with edge element FEM (in which ε_r, μ_r, ε_0 and k_0 are relative permittivity, relative permeability, permittivity in free space and propagation constant) (Firoozabadi and Miller 2010).

$$\nabla \times \mu_r^{-1}(\nabla \times \mathbf{E}) - k_0^2\left(\varepsilon_r - \frac{\mathrm{i}\sigma}{\omega\varepsilon_0}\right)\mathbf{E} = \mathbf{0}, \tag{4.1}$$

  - COMSOL builds the numeric problem, meshes the geometry and solves the matrix differently compared to method (g) (which uses NETGEN and Matlab).
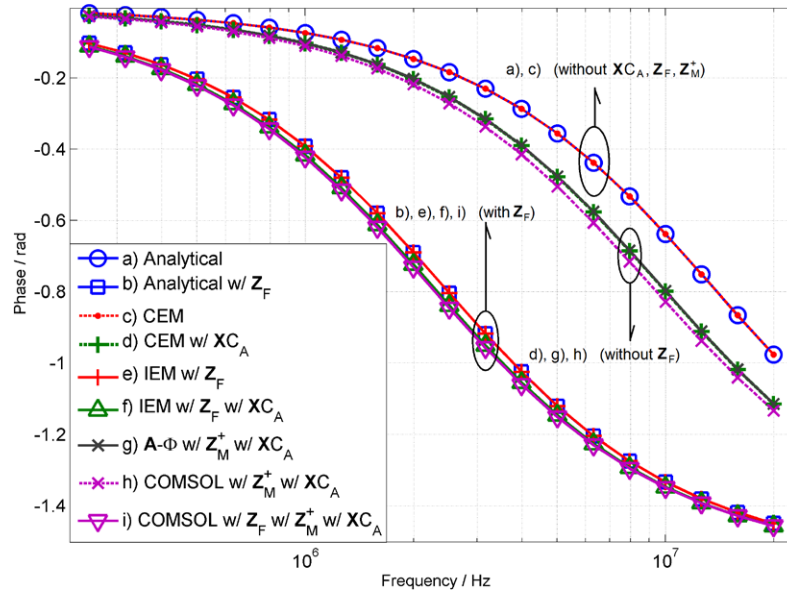
Figure 5. Solutions in phase of the forward problem obtained by using methods (a)–(i).

4.2. Tank model and discussion

For the second forward problem we use a simple cylinder tank as shown in figure 6 (relatively simple to model but complicated enough to illustrate the differences between the IEM and the other methods). There are six electrodes located at the vertical mid-point of the cylinder wall with free space surrounding the tank. Each electrode is modelled as a small circle distributed around the perimeter of the cylinder tank at a uniform 60-degree angular spacing.

Furthermore, a more realistic contact impedance is introduced in this forward problem. The electrochemical (polarization) impedance part of the contact impedance (Kolehmainen *et al* 1997) is considered. Based on experimental measurements of polarization impedance (Mirtaheri *et al* 2005), we set the contact impedance of electrodes in the Tank Model using 0.9 % -saline-gold data measured at 1 kHz. It is the highest frequency measured in the report and the experimental results suggest that the impedance tends to reduce with increasing frequency (Mirtaheri *et al* 2005), so we can expect the effect of contact impedance is less significant in the frequency range considered here. The contact impedance is given by,

$$\eta = \mathbf{Z}_C S = \left(R_C + \frac{1}{i2\pi f C_C} \right) S_C,$$

where R_C is the resistive part measured in the contact impedance experiment, C_C is the capacitive part,

$\mathbf{Z}_C$ is the measured impedance,
$f = 1$ kHz is the frequency,
S_C is the electrode surface area, 0.07 cm^2 Mirtaheri *et al* (2005).

In a similar fashion to the Lumped Model described previously, we use several methods to solve the forward problem, and make cross-comparisons to verify the results obtained from IEM, subject to the following effects,
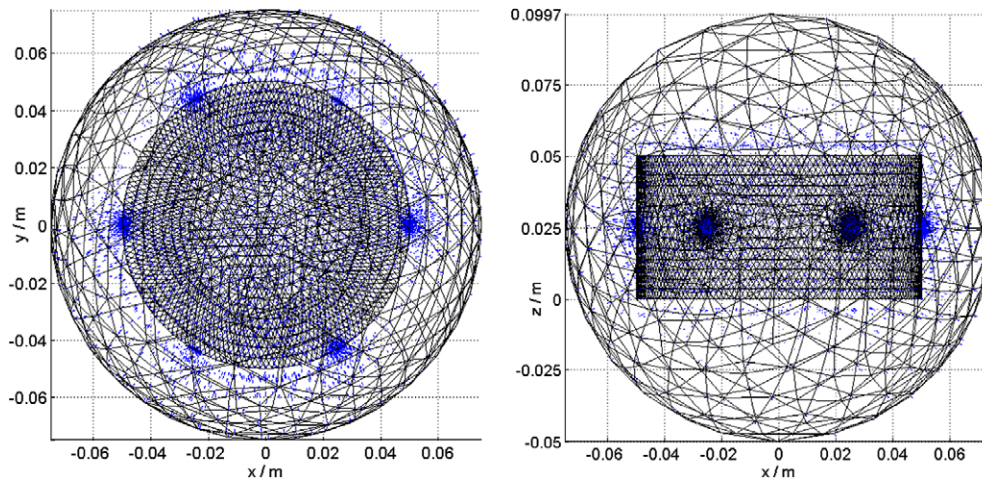
Figure 6. the geometry setting of Tank model.

- Instrumental effect, $\mathbf{Z}_F$;
- Volume Cut-off effect, $\mathbf{XC}_A$;
- Full Maxwell's effect, $\mathbf{Z}_{M^+}$.

Figure 7 illustrates the equivalent circuit for the Tank Model. A pair of ideal current sources are attached to two electrodes of the tank. Each of these sources comes with its instrumental impedance $\mathbf{Z}_{FD}$, consisting of R_F and C_{FD}. The sources drive the tank through the contact impedance η_D (expressed as an impedance $\eta_D S^{-1}$ where S is the electrode surface area). The impedances $\eta_D S^{-1}$ are shown with dashed lines, as the true locations are at the surface of the electrodes. Two electrodes (No. 4 and No. 5 on the right hand side) constitute the measurement circuit with the differential voltage between them (DV$_{45}$) measured down-stream from the contact impedance ($\eta_M S^{-1}$) and with their instrumental impedance attached ($\mathbf{Z}_{FM}$ to ground comprising R_F and C_{FM} in parallel). The model includes instrumental impedances for all six electrodes ($\mathbf{Z}_{FM}$ for measuring and $\mathbf{Z}_{FD}$ for driving) although these are not all shown on the diagram. Once again the model uses simplistic equivalent impedance representations for the volume cut-off effect (represented by capacitor C_A) and the full Maxwell effect (represented by the two port network $\mathbf{Z}_{M^+}$). In simulations, the driving and measuring pattern can be varied to use any of the available electrode pairs.

We obtained the results using the following solution methods:

(a) CEM using EIDORs;
(b) CEM including the outer free space using EIDORs;
(c) IEM including the outer free space and instrumental effects;
(d) $\mathbf{A} - \Phi$ forward model in Helmholtz equations;
(e) COMSOL without the instrumental effect;
(f) COMSOL including the instrumental effect.

The model parameters are:

- Material conductivity, 0.03 S m^{-1};
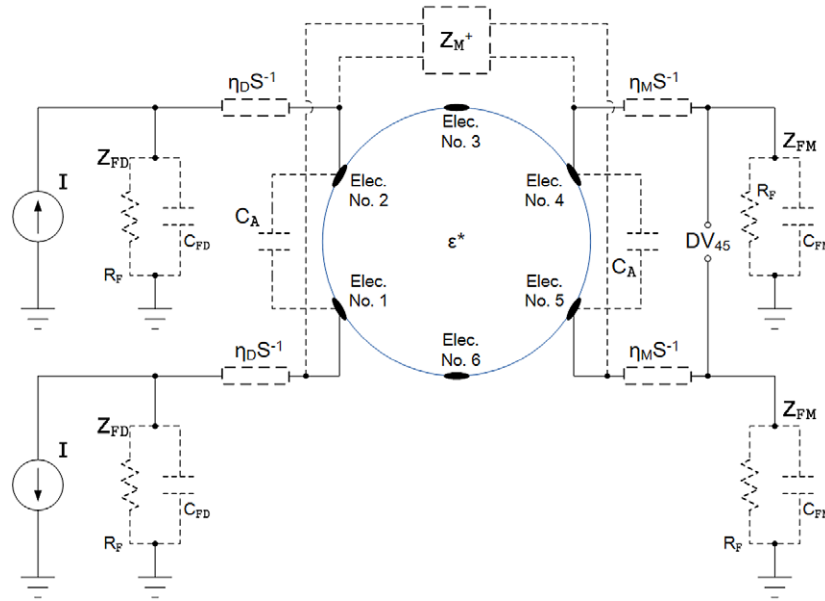- Material relative permittivity, 40;

Figure 7. Equivalent circuit of Tank Model including instrumental effects.

- Tank radius, 0.05 m;
- Tank height, 0.05 m;
- Electrode radius, 0.002 m;
- Driving current, 1 mA;
- An electrode drive pattern based on opposite driving (1 and 4) and measuring electrodes (2 and 5) is used.

Together with some parameters which apply to particular solution methods,

- For method (c), R_F = 5 MΩ, C_{FD} (the capacitive part of the instrumental impedance on driving electrodes) = 10 pF, and C_{FM} (the capacitive part of the instrumental impedance on measuring electrodes) = 6 pF.
- The diameter of the free space sphere in methods (b)–(f) is 0.15 m.
- The BC used in (d), $A - \Phi$ forward model, is similar to the Gap electrode model Boyle and Adler (2011) (see appendix) and does not include the contact impedance or instrumental impedance.
- Contact impedance is not applicable in COMSOL Electromagnetic simulation, and is not applied in methods (e) and (f).
- For methods (a)–(c), the contact impedance on measuring electrodes,

$$\eta_M = 7 \times 10^{-4} - i5 \times 10^{-4}, \Omega \cdot m^2.$$

- For methods (a)–(c), the contact impedance on driving electrodes,

$$\eta_D = 1 \times 10^{-6}, \Omega \cdot m^2.$$

Table 2 summarises the methods we used.

For all three methods the contact impedance of the driving electrodes is set to the same small value used for the Lumped Model, so that the measured voltage difference is comparable with

Table 2. List of the effects considered by each method.

Index	Name	Contact Impedance η_D	η_M	Effect $\mathbf{Z}_F$	Effect $\mathbf{XC}_A$	Effect $\mathbf{Z}_{M^+}$
(a)	CEM	Small	**Yes**	No	No	No
(b)	CEM w/$\mathbf{XC}_A$	Small	**Yes**	No	**Yes**	No
(c)	IEM w/$\mathbf{XC}_A$	Small	**Yes**	**Yes**	**Yes**	No
(d)	$\mathbf{A} - \Phi$	No	No	No	**Yes**	**Yes**
(e)	COMSOL	No	No	No	**Yes**	**Yes**
(f)	COMSOL w/$\mathbf{Z}_F$	No	No	**Yes**	**Yes**	**Yes**

methods (d)–(f) which do not include contact impedance (The contact impedance on driving electrodes is in series with the impedance of the whole tank, which reduces the current flowing through the driving electrodes when a finite instrumental impedance is present at the electrodes.). The contact impedance on the driving electrodes exacerbates the instrumental effects but here we ignore it to show the instrumental effects caused by the measuring electrodes.

Figures 8 and 9 show magnitude and phase for the measured differential voltage for methods (a)–(f) (driving at electrode No. 1 and 4 and measuring at No. 2 and 5).

From figures 8 and 9 we found:

- The volume cut-off effect, $\mathbf{XC}_A$, due to the free space surrounding the tank, is not easily observed until the frequency exceeds 5 MHz. See curves (a) and (b).
- The full Maxwell effect, $\mathbf{Z}_{M^+}$, is not easily observed until the frequency exceeds 5 MHz. See curves (b), (d) and (e).
- The instrumental effect, $\mathbf{Z}_F$, can be easily observed from $f > 300$ kHz. See curves (b), (c) and (f).
- The observed discrepancy between (d) and (e) may be due to numerical differences in the methods for $\mathbf{A} - \Phi$ and COMSOL (as discussed previously for the Lumped Model).
- The difference between (c) and (f) could result from a combination of the full Maxwell effect, lack of contact impedance in (f) and differences in numerical methods (different mesh, nodal/edge elements, solver, etc.), but it is not significant.
- Results (e) and (f) obtained using COMSOL do not converge for frequencies lower than 2 MHz (3 MHz for (f)). These results illustrate the limitations of COMSOL.

It is desirable to check at high frequencies whether the Laplace equation with our IEM model is adequate to predict the potential distribution without resorting to the full Maxwell equations, especially at frequencies where the quasi-static hypothesis tends to fail. In other words, we check here whether the instrumental effect is the effect dominates the full Maxwell effect across the frequency range of interest.

Figures 10 and 11 show contour plots (logarithmic scale) for the electric potential obtained by different methods with opposite and adjacent electrode drive at $f = 5.01$MHz. The three subplots illustrate results for (*a*) the $\mathbf{A} - \Phi$ method, (*b*) CEM with $\mathbf{XC}_A$ and (*c*) IEM.

In figures 10 and 11, the contours are at z = 0.025 m (electrodes slice, see figure 6). The edge of the tank is in blue. The green dots in the plots represent electrodes and the red ones represent the driving electrodes.

The electric potentials obtained using the $\mathbf{A} - \Phi$ and CEM methods are similar, whereas the IEM method produces different results. It suggests the Maxwell effect does not contribute to the difference as much as the instrumental effect does for the parameters we chose. Hence if the instrumental effect is taken into account then the Laplace equations as implemented by the IEM should be used to predict the potential distribution.
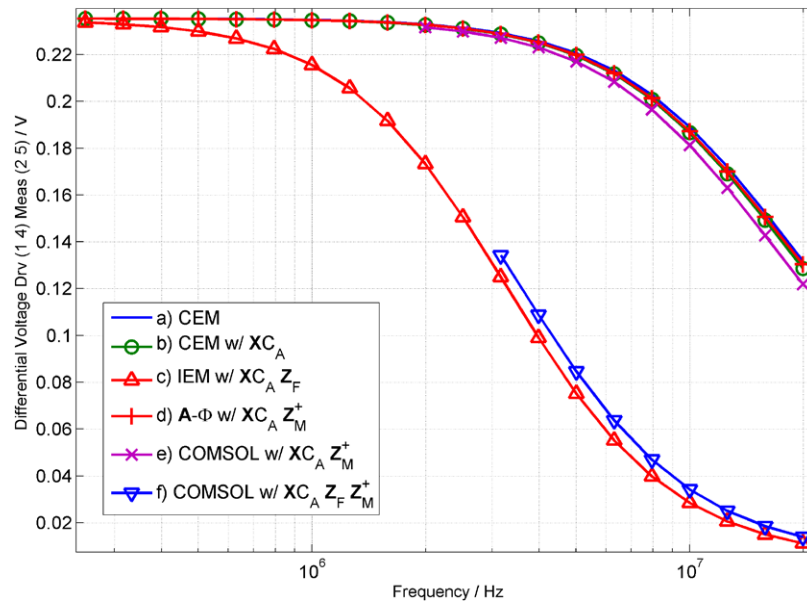
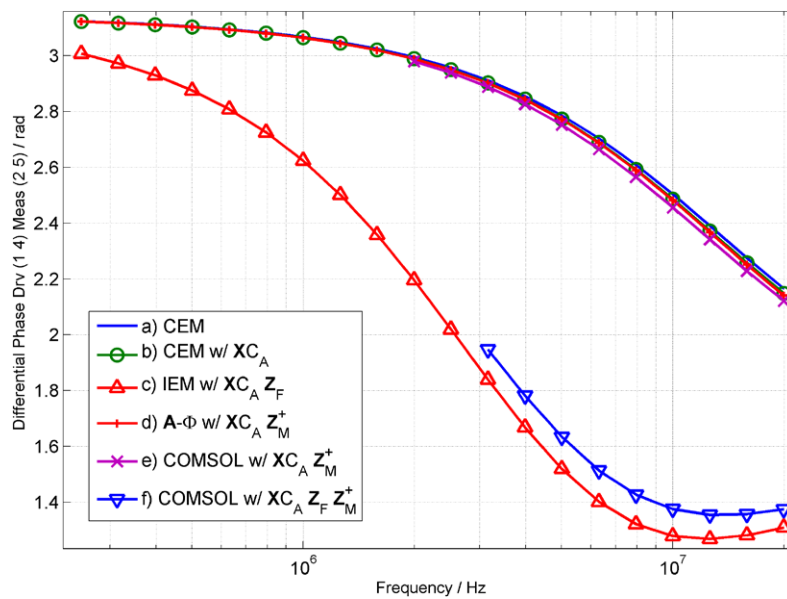**Figure 8.** Voltage difference (magnitude) on measuring electrodes.

Figure 9. Voltage difference (phase) on measuring electrodes.

5. Summary

This paper investigates the effects of non-ideal instrumentation on the performances of EIT front-end hardware. A more accurate electrode model for forward problems, IEM, is presented which includes the instrumental loading effects in the electrode model. We conclude that *the instrument loading effects should be considered by both semi Maxwell and full Maxwell*
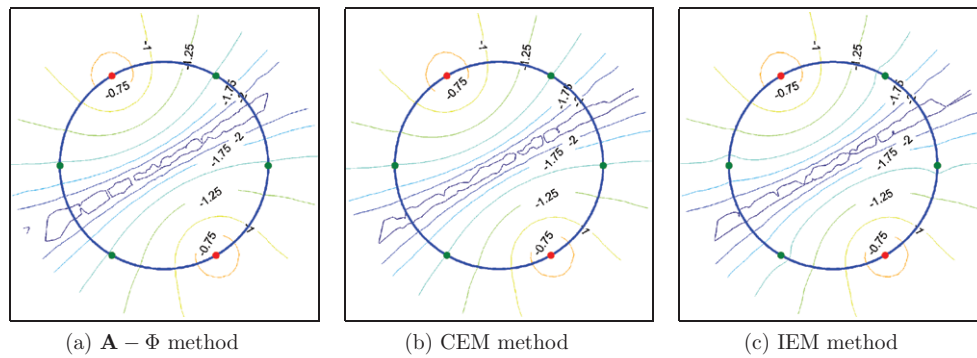
(a) $\mathbf{A} - \Phi$ method   (b) CEM method   (c) IEM method

Figure 10. Contours of potential with opposite electrode drive at frequency 5.01 MHz. (*a*) the $\mathbf{A}-\Phi$ method. (*b*) CEM method. (*c*) IEM method.
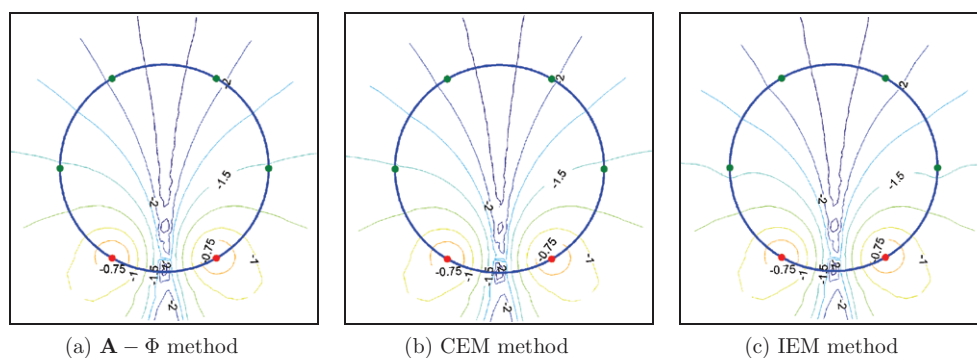

(a) $\mathbf{A} - \Phi$ method   (b) CEM method   (c) IEM method

Figure 11. Contours of potential with adjacent electrode drive at frequency 5.01 MHz. (*a*) the $\mathbf{A}-\Phi$ method. (*b*) CEM method. (*c*) IEM method.

methods, and the full Maxwell results (using the COMSOL with instrumental boundary conditions; see figures 8 and 9) confirm our argument.

Modelling demonstrates that the IEM model provides a more accurate representation in the frequency range from 500 kHz to a few MHz, a range where it is difficult for GIC circuits to overcome instrument effects at the driving electrodes and for calibration methods to compensate for effects at the measuring electrodes. Simulations show that an IEM formulation of the semi-Maxwell equations can provide a more accurate solution for the forward problems in situations where the full Maxwell effect is not the dominant effect in the frequency range. It is suggested to check with full Maxwell's solvers whether the material and frequency is suitable for the Laplace equations.

Table 3 summarises the general characteristics of the various solution methods investigated in this paper.

It is worth noting that the beta dispersion frequency used in some studies for distinguishing cancerous from normal tissues is reported to be fall in the same frequency range (100 kHz to 10 MHz) (Grimnes and Martinsen 2008, Schwan 1957, Surowiec *et al* 1988).

The IEM is a model for including instrumental effects in the electrode model to be solved with the forward problems, rather than a formula applied to a specific hardware setting. This concept can be applicable to different EIT systems by identifying major front-end non-idealities and including their impacts in the forward problems.

Table 3. Comparison of general characteristics of different methods for solving the forward problems.

	Analytical	CEM	IEM	$\mathbf{A}-\Phi$ method	COMSOL
Inversion	No	**Capable**	**Capable**	**Capable**	Difficult
Instrumental effect	**Yes**	No	**Yes**	No	**Yes**
Maxwell's effect	No	No	No	**Yes**	**Yes**
Complicated geometry & outer space	No	**Yes**	**Yes**	**Yes**	**Yes**
Processing density	Low	Normal	Normal	**High**	**High**
Low frequency stability	**Good**	**Good**	**Good**	**Good**	Poor
High frequency Accuracy	Normal	Poor	Material Dependant	Material Dependant	**Good**

For effective use of the EIT model it is important to quantify the instrumental impedance present on each electrode. Approaches to characterisation of EIT hardware are currently under investigation and will facilitate the application of a more accurate forward model. Related inverse methods for the IEM and the use of instrumental boundary conditions for full Maxwell solvers are also the subject of further investigation, and the results will appear soon.

Appendix A.

This section describes our derivation of the $\mathbf{A}-\Phi$ Helmholtz equation from the full Maxwell equations. The $\mathbf{A}-\Phi$ formulation is used in section 4 as comparative solution method.

Our work on the $\mathbf{A}-\Phi$ problem is based on the reports (Boyse *et al* 1992, Boyse and Paulsen 1997, Paulsen *et al* 1992, Soni *et al* 2006). Compared with the 2D work (Soni *et al* 2006), we develop a 3D model with the data structure provided by EIDORS and element meshing provided by NETGEN.

We have derived the coupled equations arising from Maxwell's equations in our earlier description of the forward problem (see equation (2.3) and equation (2.4)). Using equation (2.1a), equation (2.1b) and equation (2.3) we have,

$$\nabla \times \frac{1}{\mu}\nabla \times (-\nabla\Phi - i\omega\mathbf{A}) + i\omega\varepsilon^*(-\nabla\Phi - i\omega\mathbf{A}) = 0.$$

With equation (2.4), we obtain,

$$\nabla \times \frac{1}{\mu}\nabla \times \mathbf{A} + \varepsilon^*(i\omega\mathbf{A} + \nabla\Phi) = 0, \tag{A.1a}$$

$$\nabla \cdot \varepsilon^*(i\omega\mathbf{A} + \nabla\Phi) = 0. \tag{A.1b}$$

Note, the vector potential $\mathbf{A}$ and scalar potential Φ are not defined uniquely, and the Lorentz Gauge says

$$\nabla \cdot \mathbf{A} = -\varepsilon^*\mu\Phi. \tag{A.2}$$

Furthermore, the $\mathbf{A}-\Phi$ strong formula is given as,

$$\nabla \times \frac{1}{\mu}\nabla \times \mathbf{A} + i\omega\varepsilon^*\mathbf{A} - \nabla\frac{1}{\mu}\nabla \cdot \mathbf{A} - \Phi\nabla\varepsilon^* = 0, \tag{A.3a}$$

$$\varepsilon^{*2}\mu\Phi - \frac{1}{i\omega}\nabla\cdot\varepsilon^*\nabla\Phi - \mathbf{A}\cdot\nabla\varepsilon^* = 0. \tag{A.3b}$$

With the arbitrary test function ψ added, and the gradient of material properties removed by carefully chosen integral by parts, the weak formula is obtained. And using Galerkin's method, domain discretization and linear shape functions, $\Phi = \sum_{j=1}^{N}\phi_j\nu_j$, $\mathbf{A} = \sum_{j=1}^{N}\phi_j\mathbf{\Lambda}_j$ and $\psi = \phi_i$ we have

$$\sum_{j=1}^{N}\frac{1}{\mu}\int_{\Omega}\nabla\phi_i\cdot\nabla\phi_j dV\mathbf{\Lambda}_j - \sum_{j=1}^{N}\frac{1}{\mu}\int_{\Omega}(\nabla\phi_i\cdot\mathbf{\Lambda}_j)\nabla\phi_j dV + \sum_{j=1}^{N}\frac{1}{\mu}\int_{\Omega}(\nabla\phi_j\cdot\mathbf{\Lambda}_j)\nabla\phi_i dV$$

$$+ \sum_{j=1}^{N}i\omega\varepsilon^*\int_{\Omega}\phi_i\phi_j dV\mathbf{\Lambda}_j + \sum_{j=1}^{N}\varepsilon^*\nu_j\int_{\Omega}\phi_i\nabla\phi_j dV + \sum_{j=1}^{N}\varepsilon^*\nu_j\int_{\Omega}\phi_j\nabla\phi_i dV$$

$$= -\oint_{\partial\Omega}\hat{\mathbf{n}}\times\phi_i\frac{1}{\mu}\nabla\times\mathbf{A}dS + \oint_{\partial\Omega}\left(\phi_i\frac{1}{\mu}\nabla\cdot\mathbf{A}\right)\hat{\mathbf{n}}dS + \oint_{\partial\Omega}(\varepsilon^*\phi_i\Phi)\hat{\mathbf{n}}dS, \tag{A.4a}$$

$$\sum_{j=1}^{N}\varepsilon^{*2}\mu\nu_j\int_{\Omega}\phi_i\phi_j dV + \sum_{j=1}^{N}\frac{1}{i\omega}\varepsilon^*\nu_j\int_{\Omega}\nabla\phi_i\cdot\nabla\phi_j dV + \sum_{j=1}^{N}\varepsilon^*\int_{\Omega}\phi_i\nabla\phi_j dV\cdot\mathbf{\Lambda}_j$$

$$+ \sum_{j=1}^{N}\varepsilon^*\int_{\Omega}\phi_j\nabla\phi_i dV\cdot\mathbf{\Lambda}_j = \oint_{\partial\Omega}\varepsilon^*(\phi_i\mathbf{A}\cdot\hat{\mathbf{n}})dS + \frac{1}{i\omega}\oint_{\partial\Omega}\phi_i(\varepsilon^*\nabla\Phi\cdot\hat{\mathbf{n}})dS. \tag{A.4b}$$

For the boundary conditions, it is difficult to apply complex BCs used for the CEM or IEM to the $\mathbf{A}-\Phi$ problem and it is not within the scope of this paper. The BCs we used to obtain the results in section 4 are very similar to the Gap electrode model (Boyle and Adler 2011) and errors introduced by the quasi-static approximation (or the full Maxwell effect, as we named it in the previous sections) can therefore be estimated independently and separately from any errors caused by electrode models.

The Lorentz gauge appears in the normal component on the RHS of equation (A.4a), and as it holds, the normal condition vanishes,

$$\oint_{\partial\Omega}\left(\phi_i\frac{1}{\mu}\nabla\cdot\mathbf{A}\right)\hat{\mathbf{n}}dS + \oint_{\partial\Omega}(\varepsilon^*\phi_i\Phi)\hat{\mathbf{n}}dS = 0.$$

For the tangential components,

$$-\oint_{\partial\Omega}\hat{\mathbf{n}}\times\phi_i\frac{1}{\mu}\nabla\times\mathbf{A}dS = -\oint_{\partial\Omega}\phi_i\hat{\mathbf{n}}\times\mathbf{H}dS. \tag{A.5}$$

And the RHS of equation (A.4b) can be reduced to a scalar condition of the E field,

$$\oint_{\partial\Omega}\varepsilon^*(\phi_i\mathbf{A}\cdot\hat{\mathbf{n}})dS + \frac{1}{i\omega}\oint_{\partial\Omega}\phi_i(\varepsilon^*\nabla\Phi\cdot\hat{\mathbf{n}})dS$$

$$= -\frac{1}{i\omega}\oint_{\partial\Omega}\phi_i(\varepsilon^*\mathbf{E}\cdot\hat{\mathbf{n}})dS. \tag{A.6}$$

By assuming that the electromagnetic field at the boundary of the outer free space is relatively small, we force equations (A.5) and (A.6) to vanish, and since the boundary is well outside the main imaging volume (as seen in the Lumped Model or Tank Model), we assume that numeric chopping or reflection does not introduce significant

errors. (Coordinate transformations between the global geometry system and the boundary geometry system have been performed in order to apply Dirichlet conditions on equation (A.5)).

For the electrode surfaces, we derive the BCs as shown below where subscript 1 denotes the inner surface and subscript 2 denotes the outer surface (in the metal electrode). The tangential component of the electric field should be continuous so

$$(\mathbf{E}_1 - \mathbf{E}_2) \times \hat{\mathbf{n}} = \mathbf{0}.$$

Also the electric field does not exist in the metal,

$$\mathbf{E}_2 = \mathbf{0} \quad (\varepsilon_2 \approx \varepsilon_0 \neq \infty).$$

Current conservation yields,

$$\nabla \cdot (\mathbf{J}_2 + \mathbf{J}_1) = \nabla \cdot (\mathbf{J}_2 + \sigma_1 \mathbf{E}_1) = -\mathrm{i}\omega\rho.$$

So we can express the BC of equation (A.6) as

$$\mathbf{J}_n = \mathbf{J}_2 \cdot \hat{\mathbf{n}} = -(\sigma_1 \mathbf{E}_1 + \mathrm{i}\omega\varepsilon_1 \mathbf{E}_1) \cdot \hat{\mathbf{n}} = -\varepsilon_1^* \mathbf{E}_1 \cdot \hat{\mathbf{n}},$$

$$\frac{1}{\mathrm{i}\omega} \oint_{\partial\Omega} \psi\left(\varepsilon_1^* \mathbf{E}_1 \cdot \hat{\mathbf{n}}\right) \mathrm{d}S = \frac{1}{\mathrm{i}\omega} \oint_{\partial\Omega} \psi \mathbf{J}_n \mathrm{d}S,$$

where $\mathbf{J}_n$ is the normal current density at the driving electrodes and is zero elsewhere Furthermore, the current density is replaced by the injected current with a constant factor derived from an integral of the shape function.

Appendix B.

As mentioned in section 3.1, the IEM formula needs to be revised for voltage source EIT systems, and we derive it here including a simple example. Theoretically, there is no difference between voltage source and current source EIT systems, as voltage sources and current sources can be made equivalent in circuits. However, using voltage source systems can avoid the situation where current source systems are not able to provide output impedance high enough to avoid from loading effects (Holder 2005).

Although voltage source EIT systems can bring some benefits, the non-idealities, however, cannot be completely avoided. First, the input impedance between the voltage measuring electrode pairs cannot be infinite. Second, voltage source systems need to measure the currents on the exciting electrodes as it appears in inverse problems (Holder 2005), but the current measurements can be inaccurate due to the finite impedance attached to electrodes.

Different approaches have been used for implementing EIT systems with voltage sources, including resistive sensors (Halter *et al* 2008, Saulnier *et al* 2006), bridges (Dutta *et al* 2001, Li *et al* 2013), etc. Typically, the voltage source system can be modelled as a collection of voltage sources, current measurement and voltage measurement components. We use figure B1 to explain this, which is modified from figure 1.

The switch controls the electrode to be in the exciting mode or measuring mode. In the exciting mode, an ideal voltage source is assumed and applied, generating a voltage V_{Sl}. A small resistor (connected between the source and the electrode) is used to measure the injected current. Similar to current source systems, not all the current measured by the sensor goes into the electrode especially when the operating frequency is high due to the finite impedance attached to electrode (measurement circuit, switches and parasitic capacitor, etc.). These non-ideal instrumental effects result in inaccuracy. In the measuring mode, there are

leakage currents flowing throughout the electrode and perturbing the potential distribution in the volume in a way similar to current source systems.

To derive the forward model for voltage source systems, the same procedure as in section 3.1 is used. We apply the current equation for the circuit node E to obtain,

$$\frac{V_l - V_{Sl}}{\mathbf{Z}_S} + \frac{V_l - V_{GND}}{\mathbf{Z}_F} + I_l = 0, \quad \text{in the driving mode,}$$

and,

$$\frac{V_l - V_{GND}}{\mathbf{Z}_F} + I_l = 0, \quad \text{in the measuring mode,}$$

where $\mathbf{Z}_S$ denotes the sensing impedance of each electrode. Combining these two equations, we obtain (with $\mathbf{Z}_S = \infty$ indicating the measuring mode),

$$\left(\frac{1}{\mathbf{Z}_S} + \frac{1}{\mathbf{Z}_F}\right) V_l + I_l = \frac{V_{Sl}}{\mathbf{Z}_S}. \tag{B.1}$$

Substituting the above equation into the weak formula, we have,

$$\int_\Omega \varepsilon^* \nabla v \cdot \nabla \Phi \mathrm{d}V + \sum_{l=1}^{L} \frac{1}{\eta} \int_{S_l} v \Phi \mathrm{d}S - \sum_{l=1}^{L} \frac{V_l}{\eta} \int_{S_l} v \mathrm{d}S = 0,$$

$$\int_{S_l} \frac{V_l - \Phi}{\eta} \mathrm{d}S - I_l = 0,$$

$$\left(\frac{1}{\mathbf{Z}_{Sl}} + \frac{1}{\mathbf{Z}_{Fl}}\right) V_l + I_l = \frac{V_{Sl}}{\mathbf{Z}_{Sl}}, \qquad l = 1, 2, \cdots L - 1,$$

$$\left(\frac{1}{\mathbf{Z}_{SL}} + \frac{1}{\mathbf{Z}_{FL}}\right) V_L - \sum_{l=1}^{L-1} I_l = \frac{V_{SL}}{\mathbf{Z}_{SL}}. \tag{B.2}$$

With $\mathbf{Z}_S = [\mathbf{Z}_{S1}, ..., \mathbf{Z}_{SL}]^T$ and $v_S = [V_{S1}, ..., V_{SL}]^T$ the FEM matrix can be,

$$\begin{pmatrix} A + B & C & \mathbf{0}^{N \times L} \\ C^T & D & -\mathbb{I}^{L \times L} \\ \mathbf{0}^{L \times N} & G & F \end{pmatrix} \begin{pmatrix} \mathbf{u} \\ \mathbf{v} \\ \mathbf{i} \end{pmatrix} = \begin{pmatrix} \mathbf{0}^{N \times 1} \\ \mathbf{0}^{L \times 1} \\ \mathbf{v}_S / \mathbf{Z}_S \end{pmatrix},$$

$$G = \mathrm{diag}\left\{\frac{1}{\mathbf{Z}_S} + \frac{1}{\mathbf{Z}_F}\right\}, \in \mathbb{C}^{L \times L}.$$

In the measuring mode, $1/\mathbf{Z}_{Sl}$ is set to zero. The formula is very similar to the current source IEM but more complicated than the voltage source CEM. In addition, it predicts the current on the sensing resistor, but it requires the information of instrumental impedance $\mathbf{Z}_F$ and sensing impedance $\mathbf{Z}_S$.

We use the tank model in section 4.2 with the following parameters to show the difference between the voltage source CEM and the voltage source IEM.

- Driving Voltages: +/− 2 V;
- An electrode-driving pattern based on the opposite driving (1 and 4) and measuring electrodes (2 and 5) is used;
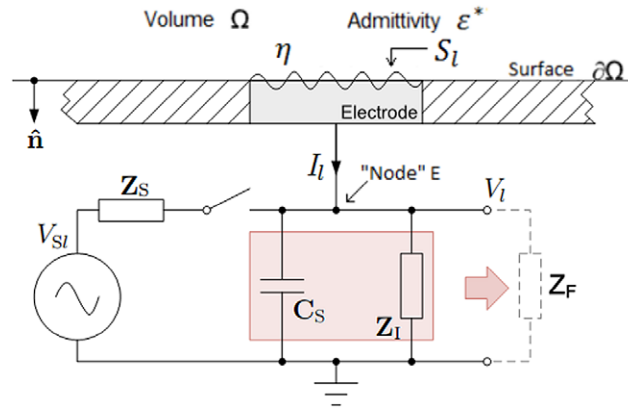
Figure B1. EIT electrode geometry and voltage source circuit model, where V_{Sl} is the voltage generated by the source, connected with the lth electrode, $\mathbf{Z}_S$ is the impedance of the sensor resistor. For the remaining symbols in the figure we kept the previous definitions.
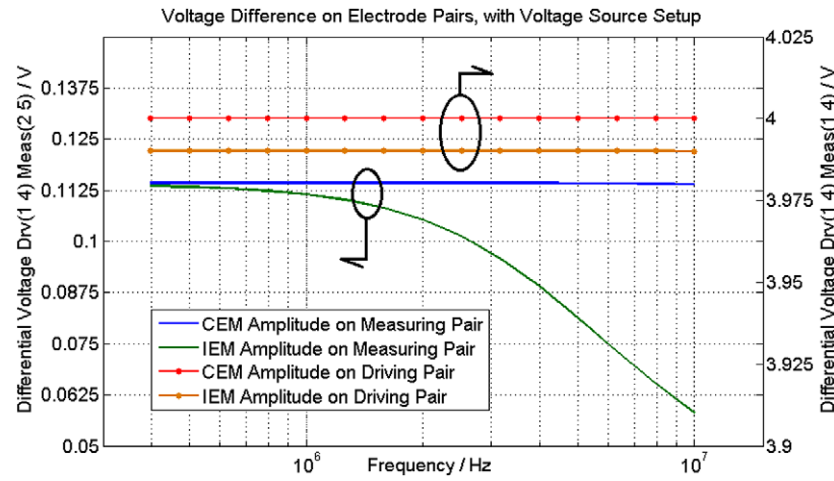

Figure B2. Voltage difference on electrode Pairs, with voltage source setup.

- In order for comparison, the voltage across the driving electrode pair is monitored;
- For IEM $R_F = 5$ MΩ, $C_{FM} = C_{FM} = 6$ pF, and $\mathbf{Z}_S = 10$ Ω for voltage driving electrodes;
- The contact impedance on both driving and measuring electrodes,

$$\eta = 7 \times 10^{-4} - \text{i}5 \times 10^{-4}, \Omega \cdot \text{m}^2 \,.$$

Simulation results are shown in figure B2. The instrumental effect on driving electrodes, contributed by the measuring circuits and parasitic capacitors, is not significant. The difference between the voltages on the CEM driving pair (red dot curve) and the IEM driving pair (orange dot curve) is caused by the sensor impedance, and we ignore it for simplicity here. On the other hand, it suggests that the CEM solutions can be significantly inaccurate on the measuring electrode pairs due to the instrumental effects. The CEM shows an almost constant voltage across the frequency band (blue curve), whereas the IEM concludes that the input

impedance of the measuring pair varies with frequency (green curve), and it changes the potential distribution inside the object accordingly.

Furthermore, the current measurements in the voltage source systems affected by hardware non-idealities can be more serious than what the simulation shows, especially when the sensing impedance contains a significant capacitive component. This problem is system dependent and closely related to the inverse problem, but we would like to discuss it in a different report.

Acknowledgments

References

Adler A and Lionheart W R B 2006 Uses and abuses of EIDORS: an extensible software base for EIT *Physiol. Meas.* **27** 25–42

Ahn S, Oh T I, Jun S C, Lee J, Seo J K and Woo E J 2010 Weighted frequency-difference EIT measurement of hemisphere phantom *J. Phys.: Conf. Ser.* **224** 012161

Barber D C and Brown B H 1984 Applied potential tomography *J. Phys. E: Sci. Instrum.* **17** 723–33

Boverman G, Kim B, Isaacson D and Newell J C 2007 The complete electrode model for imaging and electrode contact compensation in electrical impedance tomography Proc. 29th Annual Int Conf. of the IEEE Engineering in Medicine and Biology Society (EMBS) (Lyon, Aug. 2007) p 34623465

Boyle A and Adler A 2010 Electrode models under shape deformation in electrical impedance tomography *J. Phys.: Conf. Ser.* **224** 012051

Boyle A and Adler A 2011 The impact of electrode area, contact impedance and boundary shape on EIT images *Physiol. Meas.* **32** 745–54

Boyse W E, Lynch D R, Paulsen K D and Minerbo G N 1992 Nodal-based finite-element modeling of Maxwell's equations *IEEE Trans. Antennas Propag.* **40** 642–51

Boyse W E and Paulsen K D 1997 Accurate solutions of Maxwell's equations around PEC corners and highly curved surfaces using nodal finite elements *IEEE Trans. Antennas Propag.* **45** 1758–67

Cheney M, Isaacson D and Newell J C 1999 Electrical impedance tomography *SIAM Rev.* **41** 85–101

Cheng K S, Isaacson D, Newell J C and Gisser D G 1989 Electrode models for electric current computed tomography *IEEE Trans. Biomed. Eng.* **36** 918–24

Demidenko E 2011 An analytic solution to the homogeneous EIT problem on the 2D disk and Its application to estimation of electrode contact impedances *Physiol. Meas.* **32** 14531471

Demidenko E, Borsic A, Wan Y, Halter R J and Hartov A 2011 Statistical estimation of EIT electrode contact impedance using a magic Toeplitz matrix *IEEE Trans. Biomed. Eng.* **58** 2194–201

Denyer C W, Lidgey F J, Zhu Q S and McLeod C N 1994 A high output impedance current source *Physiol. Meas.* **15** A79–82

Dutta M, Rakshit A and Bhattacharyya S N 2001 Development and study of an automatic AC bridge for impedance measurement *IEEE Trans. Instrum. Meas.* **50** 10481052

Firoozabadi R and Miller E L 2010 Finite element modeling of electromagnetic scattering for microwave breast cancer detection The COMSOL Conference (Boston, Aug. 2010)

Grimnes S and Martinsen O 2008 Bioimpedance and bioelectricity basics *Bioimpedance and Bioelectricity Basics* (Amsterdam: Elsevier)

Halter R, Hartov A and Paulsen K D 2004 Design and implementation of a high frequency electrical impedance tomography system *Physiol. Meas.* **25** 379–90

Halter R, Hartov A and Paulsen K D 2008 A broadband high-frequency electrical impedance tomography system for breast imaging *IEEE Trans. Biomed. Eng.* **55** 650–9

Harrach B, Seo J K and Woo E J 2010 Factorization method and Its physical justification in frequency-difference electrical impedance tomography *IEEE Trans. Med. Imag.* **29** 1918–26

Hartinger A E, Gagnon H and Guardo R 2006 A method for modelling and optimizing an electrical impedance tomography system *Physiol. Meas.* **27** 51–64

Hartinger A E, Gagnon H and Guardo R 2007 Accounting for hardware imperfections in EIT image reconstruction algorithms *Physiol. Meas.* **28** 13–27

Holder D 2005 Electrical impedance tomography: methods, history, and applications *Electrical Impedance Tomography: Methods, History and Applications* (Bristol: Institute of Physics)

Jun S C, Kuen J, Lee J, Woo E J, Holder D and Seo J K 2009 Frequency-difference EIT (fdEIT) using weighted difference and equivalent homogeneous admittivity: validation by simulation and tank experiment *Physiol. Meas.* **30** 1087–99

Kolehmainen V, Vauhkonen M, Karjalainen P A and Kaipio J P 1997 Assessment of errors in static electrical impedance tomography with adjacent and trigonometric current patterns *Physiol. Meas.* **18** 289–303

Li N, Xu H, Wang W, Zhou Z, Qiao G F and Li D D U 2013 A high-speed bioelectrical impedance spectroscopy system based on the digital auto-balancing bridge method *Meas. Sci. Technol.* **24**

Lionheart W R B 2004 EIT reconstruction algorithms: pitfalls, challenges and recent developments *Physiol. Meas.* **25** 125–42

McEwan A, Romsauerova A, Yerworth R, Horesh L, Bayford R and Holder D 2006 Design and calibration of a compact multi-frequency EIT system for acute stroke imaging *Physiol. Meas.* **27** 199–210

Metherall P, Barber D C, Smallwood R H and Brown B H 1996 Three-dimensional electrical impedance tomography *Nature* **380** 509–12

Mirtaheri P, Grimnes S and Martinsen O G 2005 Electrode polarization impedance in weak NaCl aqueous solutions *IEEE Trans. Biomed. Eng.* **52** 2093–9

Oh T I, Lee K H, Kim S M, Koo H, Woo E J and Holder D 2007a Calibration methods for a multi-channel multi-frequency EIT system *Physiol. Meas.* **28** 1175–88

Oh T I, Wi H, Kim D Y, Yoo P J and Woo E J 2011 A fully parallel multi-frequency EIT system with flexible electrode configuration: KHU Mark2 *Physiol. Meas.* **32** 835–49

Oh T I, Woo E J and Holder D 2007b Multi-frequency EIT system with radially symmetric architecture: KHU Mark1 *Physiol. Meas.* **28** 183–96

Paulsen K D, Boyse W E and Lynch D R 1992 Continuous potential Maxwell solutions on nodal-based finite elements *IEEE Trans. Antennas Propag.* **40** 1192–200

Polydorides N and Lionheart W R B 2002 A Matlab toolkit for three-dimensional electrical impedance tomography a contribution to the electrical impedance and diffuse optical reconstruction software project *Meas. Sci. Technol.* **13** 1871–83

Ross A S, Saulnier G J, Newell J C and Isaacson D 2003 Current source design for electrical impedance tomography *Physiol. Meas.* **24** 509–16

Saulnier G J, Ross A S and Liu A S 2006 A high-precision voltage source for EIT *Physiol. Meas.* **27** 221236

Saulnier G J, Blue J C, Newell J C, Isaacson D and Edic P M 2001 Electrical impedance tomography *IEEE Signal Process. Mag.* **18** 31–43

Schwan H 1957 Electrical properties of tissue and cell suspensions *Adv. Biol. Med. Phys.* **5** 147–209

Seo J K, Lee J, Kim S W, Zribi H and Woo E J 2008 Frequency-difference electrical impedance tomography (fdEIT): algorithm development and feasibility study *Physiol. Meas.* **29** 929–44

Sheng X Q and Song W 2012 *Essentials of Computational Electromagnetics* (Singapore: Wiley)

Somersalo E, Cheney M and Isaacson D 1992 Existence and uniqueness for electrode models for electric current computed tomography *SIAM J. Appl. Math.* **52** 1023–40

Soni N K, Paulsen K D, Dehghani H and Hartov A 2006 Finite element implementation of Maxwell's equations for image reconstruction in electrical impedance tomography *IEEE Trans. Med. Imaging* **25** 55–61

Soleimani M, Powell C E and Polydorides N 2005 Improving the forward solver for the complete electrode model in EIT using algebraic multigrid *IEEE Trans. Med. Imag.* **24** 577–83

Surowiec A, Stuchly S, Barr J and Swarup A 1988 Dielectric properties of breast carcinoma and the surrounding tissues *IEEE Trans. Biomed. Eng.* **35** 257–63

Vauhkonen P J, Vauhkonen M, Savolainen T and Kaipio J P 1999 Three-dimensional electrical impedance tomography based on the complete electrode model *IEEE Trans. Biomed. Eng.* **46** 1150–60

Webster J G 1990 Electrical impedance tomography *Electrical Impedance Tomography* (Bristol: Adam Hilger)